minerals

MDPI

Article

Crystal Transformation of Sericite during Fluidized Roasting: A Study Combining Experiment and Simulation

Zhe Bai [1,2], Yuexin Han [1,2], Jianping Jin [1,2], Yongsheng Sun [1,2,*] and Qi Zhang [1,2]

[1] School of Resources and Civil Engineering, Northeastern University, Shenyang 110819, China
[2] National-Local Joint Engineering Research Center, High-Efficient Exploitation Technology for Refractory Iron Ore Resources, Shenyang 110819, China
* Correspondence: yongshengsun@mail.neu.edu.cn

Abstract: Fluidized roasting is an efficient method to promote vanadium extraction from V-bearing mica in shale. In this study, the transformation behavior of V-bearing sericite during fluidized roasting was explored by combining experimental detections and density functional theory (DFT) calculations. TG-MS, XRD, FTIR, and SEM-EDS were used to investigate the characteristics of the roasted sericite samples. The crystal parameters of V-bearing sericite were calculated with Materials Studio. The results showed that dehydroxylation was the main reaction during roasting, which occurred between 650 °C and 960 °C. After being roasted at 900 °C for 2 h, hydroxyls were completely removed. The calculation results show that −OH was removed between the metal ions in the sericite O-layer, which turned the hexa-coordinate of V^{3+}, Al^{3+}, and Fe^{3+} into pentacoordinate. Through electronic rearrangement, the bond lengths between two ions connected by −OH were shortened from 0.18~0.20 nm to 0.17 nm. However, some chemical bonds were grown, which indicates that they are weaker and easier to transform. In addition, twisted six-membered rings were formed with obvious angle changes on the (0 0 1) surface. Furthermore, Mulliken's overlap populations of some V-O, Al-O, and Fe-O were decreased. Therefore, dehydroxylation is a determining factor in the destruction of sericite crystals during fluidized roasting, which also promotes vanadium release from shale.

Keywords: sericite; crystal; DFT; fluidized roasting; dehydroxylation

check for updates

Citation: Bai, Z.; Han, Y.; Jin, J.; Sun, Y.; Zhang, Q. Crystal Transformation of Sericite during Fluidized Roasting: A Study Combining Experiment and Simulation. *Minerals* **2022**, *12*, 1223. https://doi.org/10.3390/min12101223

Academic Editor: Kenneth N. Han

Received: 1 September 2022
Accepted: 23 September 2022
Published: 27 September 2022

1. Introduction

Vanadium is a significant rare-metal element and strategic resource [1,2]. It has been extensively applied to the steel industry, special alloy, chemical industry, superconducting materials, vanadium batteries, and more [3–5]. There is a huge consumption of vanadium in China, but 87% of vanadium is stored in shale, which amounts to 118 million tons (estimated by V_2O_5) [6–8]. Shale is a type of carbonaceous shale with a low calorific value [9,10]. The low grade of V_2O_5 (0.13%~1.2%), complex minerals composition, and various occurrence states of vanadium are characteristics of shale [11,12]. In addition, V^{3+} often replaces the Al^{3+} in mica crystal with isomorphism. However, V_2O_3 has little solubility in acid [13], meaning vanadium is difficult to directly leach from shale. This results in low recovery, waste medicine, difficult purification, and high cost in current processes [14–16].

Common vanadium extraction processes include sodium roasting-water leaching, sodium roasting-acid leaching, calcification roasting-acid/alkali leaching, and direct acid leaching [17–20]. At present, many additives have been developed, including NaCl, Na_2CO_3, Na_2SO_4, CaO, $CaCO_3$, CaF_2, etc. [18,21,22]. The vanadium leaching rate reached 86.74% under the conditions of CaF_2:CaO = 2:3, an additive amount of 10 wt%, and roasting at 850 °C for 90 min. Additives could react with minerals to destroy crystal structures under lower temperatures, shorter time, or less acid solution [18]. Molten NaCl would rather react with silicate rocks, which results in crystal transformation and promotes vanadium dissociation. Studies confirmed that the key point of enhancing leaching efficiency

is to destroy the crystal structure of V-bearing minerals before the leaching process [23]. However, roasting with additives will cause serious pollution and consume lots of acidic or alkaline agents.

At present, blank roasting is being considered as a better choice to replace original technologies [23–25] because of its advantages, such as containing no additives, a low reagent consumption, and less pollution. The vanadium leaching efficiency in a blank roasting–acid leaching process reached 85.43% under the comparative leaching condition of 15% H_2SO_4 (v/v), 1 mL/g, 4 h, 95 ± 1 °C, and 5% CaF_2 (w/w) [19]. Previous studies have shown that the crystal structure of V-bearing muscovite was effectively destroyed by fluidized roasting, which promotes the release of vanadium [26]. However, the micro-damage mechanism of V-bearing muscovite by high-temperature fluidized roasting was lacking. Muscovite is the most widely distributed V-bearing mineral in shale, which leads to difficulty with leaching. Thus, some researchers studied the crystal parameters of V-bearing muscovite based on density functional theory (DFT) [27]. The results showed that the most plausible site of V was the octahedral structure in the O-layer of muscovite, and destroying this octahedral structure was key to enhancing the leaching rate of vanadium. Moreover, the bond parameters, bond angles, bond length, populations, and electron distribution were analyzed in substituted V-bearing muscovite [27–30]. During acid dissolution, the removal process of structural atoms in muscovite during acid leaching [31], and the removal of structural O and Al in the octahedron were also researched [32]. The structure and relative potential energy of the intermediate products were carefully calculated and described, which was valuable work.

In this study, experimental studies and density functional theory (DFT) calculations were innovatively combined to study the transformation of V-bearing sericite, which is a kind of fine V-bearing muscovite, and its crystal during fluidized roasting. TG-MS, XRD, FTIR, and SEM-EDS were used to analyze the thermolysis, chemical bonds, phase transition, and microstructure of sericite samples, respectively. Furthermore, V-bearing sericite crystals before and after dehydroxylation were constructed to intuitively demonstrate the transformation of crystal parameters, bond angle, bond length, and populations. It also explained the promoting effect of fluidized roasting from the perspective of crystal damage.

2. Materials and Methods

2.1. Materials

The sericite was obtained from Shijiazhuang Country, Hebei Province of China. In this research, pure sericite was used to substitute pure V-bearing sericite because it is difficult to obtain pure V-bearing sericite in nature. Although there are slight differences between them, their properties and structures are rather similar, which meets the requirements of this research. Figure 1 shows the results of particle size analyzed by a laser particle sizer, in which the content at −45 μm was more than 73%. The chemical compositions of sericite are presented in Table 1, which were determined by chemical analysis. As the main components of sericite, the contents of Al_2O_3, K_2O, and SiO_2 are 30.82 wt%, 10.54 wt%, and 49.25 wt%, respectively. The mineral composition of the ore sample was defined by XRD. Figure 2 shows that the characteristic peaks of sericite correspond well with that of sericite, as there are no other minerals' peaks. It indicates that this sericite is of high purity and meets the requirement of this research.

Table 1. The chemical multi-elemental analysis of sericite.

Composition	Al_2O_3	K_2O	SiO_2	Fe_2O_3	CaO	MgO	TiO_2
Content (wt%)	30.82	10.54	49.25	5.21	0.14	1.30	0.70

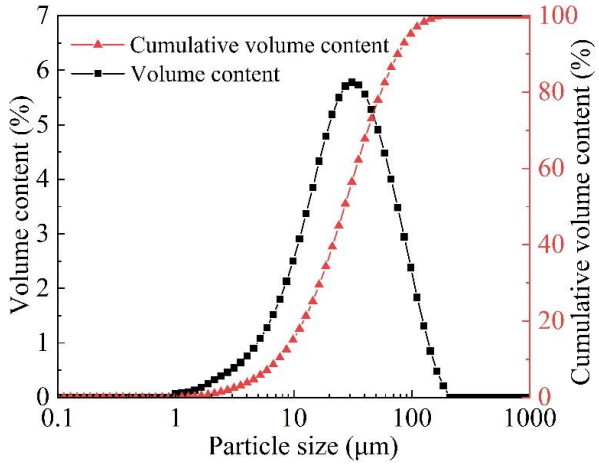

Figure 1. Particle size distribution of sericite.

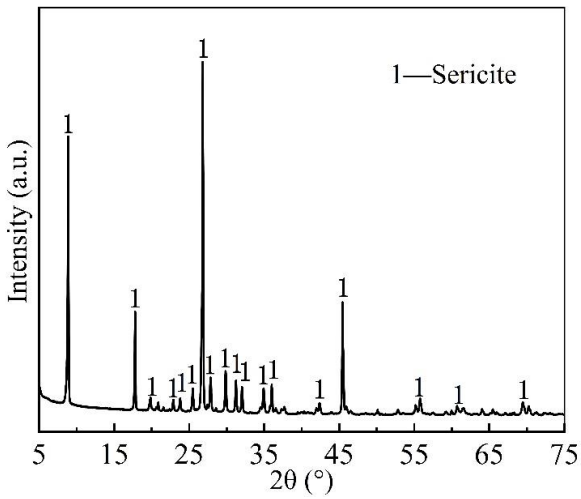

Figure 2. The XRD pattern of raw sericite.

2.2. Methods and Equipment

Figure 3 shows the schematic of the sericite fluidized roasting system. The samples were heated by vertical furnace equipment (OTF-1200X-S-VT, HF-Kejing, Hefei, China) from 25 °C to 1050 °C. A furnace tube (Φ 50 mm) with an internal breathable quartz plate was the core reactor. O_2 and N_2 gas (purity of 99.99%) supplied a flowing oxidation atmosphere controlled by rotary flowmeters (LZB-3WB, Shengzhiyuan, China). First, 20.00 g sericite was charged onto the quartz plate inside the reactor. Then, the connected furnace tube was put into the furnace cavity, which reached a set temperature. O_2 (126 mL/min) and N_2 (474 mL/min) were injected into furnace tubes. Under this condition, fluidized roasting would last for 2 h. Raw ore and roasted products were analyzed by TG-MS, XRD, FTIR, and SEM-EDS. In addition, the crystal calculation would illustrate the crystal transformation before and after roasting. Calculation parameters of the CASTAP module of Material Studio were as follows (DFT): the exchange-correlation functional selected GGA-PBE, the pseudopotential selected Ultra-soft, the cut-off energy was 400 eV, and the K-point was the Gamma point (1 × 1 × 1). This crystal structure of sericite was downloaded from the American Mineralogist Crystal Structure Database (AMCSD). Crystals of V-bearing sericite and dehydroxylated V-bearing sericite were clearly compared and analyzed in crystal parameters (bond angle, length, population, and bond strength).

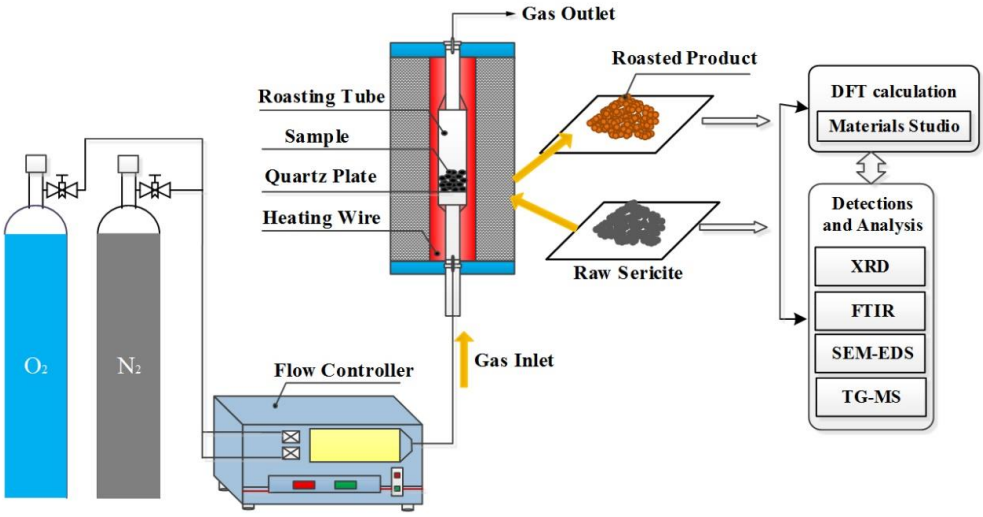

Figure 3. Schematic of sericite fluidized roasting system.

2.3. Analytical Methods

The particle size of sericite powder was determined by a laser particle sizer (Malvern Panalytical Mastersizer 3000, Malvern, UK). The phase composition of roasted products was studied by X-ray diffraction analysis (XRD, Panalytical X Pertpro, Almelo, The Netherlands). Samples were scanned within a 2θ range of 5~75°; then, the patterns were analyzed by JADE software (version 6.0, Materials Data, Newtown Square, PA, USA). Thermogravimetry combined with mass spectrometry (TG-MS, NETZSCH STA 449F3, Selb, Germany) was used to analyze the thermal decomposition process of sericite [33]. Furthermore, Fourier transforms infrared spectroscopy (FTIR, Nicolet 380, Scientific, Masyland, USA) was employed to investigate the transformations in the chemical bonds. Based on the first principle, the crystal structure of sericite was calculated using Materials Studio software (version 2019). Microstructures and elements distribution of samples were observed by scanning electron microscopy with energy dispersive spectroscopy (SEM-EDS, Zeiss Ultra Plus, Germany, and OXFORD X-MAX^N, Oxford, UK).

3. Results and Discussion

3.1. Thermal Decomposition Analysis

Thermogravimetry-mass spectrometry (TG-MS) was used to investigate the pyrolysis behavior of the sericite [34,35]. The heating rate of TG-MS is 15 °C/min under in air. As shown in Figure 4, the pyrolysis process can be divided into three stages. The first stage was from room temperature to 650 °C. The mass loss of this stage was 0.81%, which is due to the removal of some adsorbed water and crystal water [34]. Because the water content was low, changes to the TG curve and ion intensity of H_2O were small. In the second stage, from 650 °C to 960 °C, the mass loss reached 3.20%. It was demonstrated that a violent dehydroxylation reaction began at 650 °C and completely ended at 960 °C. The ion intensity of H_2O had an obvious peak in this range, revealing that the hydroxyls inside sericite crystal were removed between 650 °C and 960 °C in the form of H_2O [34,36]. Furthermore, the peak values of the DTG curve and H_2O curve were located at 850 °C and 855 °C, respectively, indicating that the maximum reaction rate occurred at 850 °C. Therefore, the effective roasting temperature for crystal damage should be above 850 °C. In contrast, the weight loss was only 0.18% at the third stage (i.e., from 960 °C to 1200 °C) because the decomposition reaction was very weak.

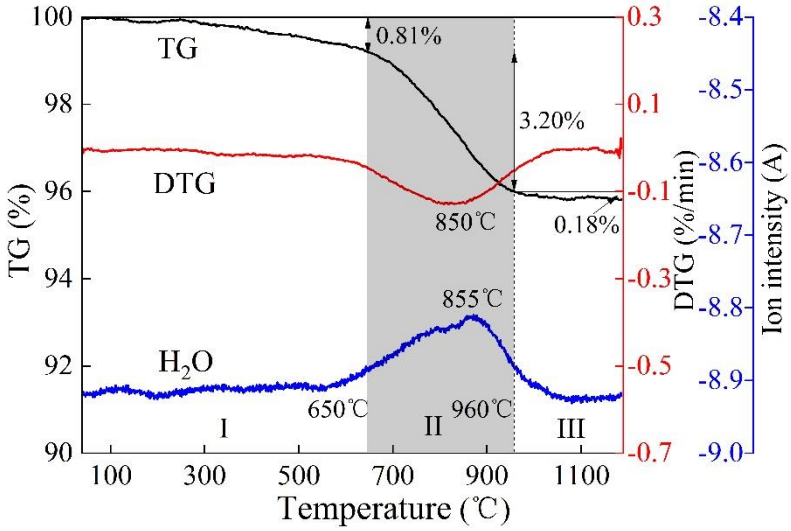

Figure 4. TG-MS analysis of raw sericite.

3.2. Transformation Behaviors of Sericite

3.2.1. Transformation of Chemical Bonds

Figure 5 shows the FTIR spectra of raw ore and roasted products (800 °C, 850 °C, 900 °C, 950 °C, and 1050 °C). Bands at 3623.23 cm^{-1} and 825.93 cm^{-1} were attributed to stretching vibrations and oscillating absorption of -OH, respectively [37,38]. Bands at 3623.23 cm^{-1} and 825.93 cm^{-1} disappeared completely when the roasting temperature reached 900 °C, indicating that the -OH in the crystal was completely removed. It was consistent with the analysis results of the TG-MS in Figure 4. In addition, $Si(Al^{IV})$-O and Si-O-$Si(Al^{IV})$ were also changed (absorption bands at 798 cm^{-1}, 748 cm^{-1}, 693 cm^{-1}, and 1027 cm^{-1}, and shoulder absorption band at 1068 cm^{-1} [37]). As shown in Figure 5b, bands at 798 cm^{-1}, 748 cm^{-1}, and 693 cm^{-1} gradually weakened and disappeared at 900 °C with the increase in temperature. The bands at 1027 cm^{-1} and 1050 cm^{-1} also moved to low and high frequency, respectively. Then, the FTIR spectra basically remained unchanged when the temperature was above 900 °C. Figure 5 illustrates the main changes in this spectrum related to -OH, $Si(Al^{IV})$-O, and Si-O-$Si(Al^{IV})$, indicating that dehydroxylation was accompanied by significant changes in $Si(Al^{IV})$-O and Si-O-$Si(Al^{IV})$ during roasting.

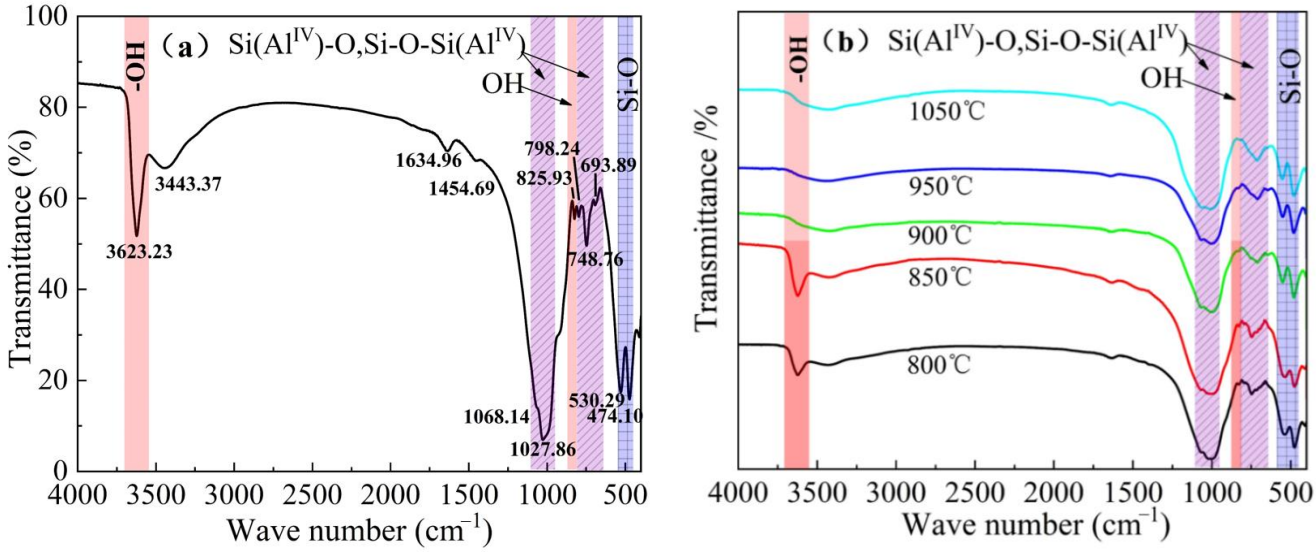

(**a**) (**b**)

Figure 5. FTIR spectra of raw ore (**a**) and roasted products (**b**).

3.2.2. Phase Transformation

The XRD patterns of sericite samples are shown in Figure 6. During fluidized roasting, the mineralogical phase changed from sericite to dehydroxylated sericite. With the increase in roasting temperature, the characteristic peaks of raw sericite at 36.1°, 45.5°, 69.6°, and 70.2° gradually weakened and then finally disappeared at 850 °C. Meanwhile, new peaks located at 35.6°, 45.0°, 64.7°, and 68.7° were attributed to the generation of dehydroxylated sericite. On the one hand, it was confirmed that the dehydroxylation reaction led to phase transformation during roasting. On the other hand, the roasting temperature should be higher than 850 °C to cause sericite crystal damage.

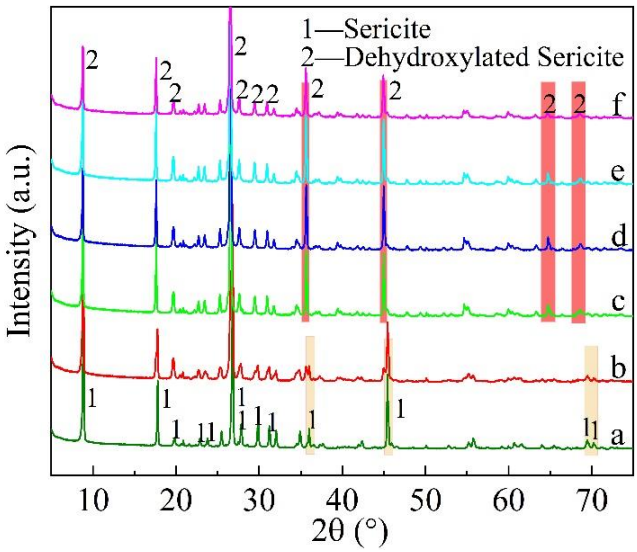

Figure 6. XRD analysis of roasted products at different temperatures (raw ore (**a**), 700 °C (**b**), 850 °C (**c**), 900 °C (**d**), 950 °C (**e**), and 1050 °C (**f**)).

To further analyze the variation in crystal planes of roasted products, the interplanar spacings of diffraction peaks were measured, and the results are shown in Table 2. The interplanar spacings of (006), (002), (004), (008), and (025) increased continuously from raw ore to 850 °C. Among them, (006), (002), and (004) were changed at 850 °C, which were the three strongest peaks of sericite located at 26.8°, 17.8°, and 8.8° along the crystal c-axis. The interplanar spacings of (006), (002), and (004) increased from 0.3323 nm, 0.9973 nm, and 0.4984 nm to 0.3354 nm, 1.0040 nm, and 0.5029 nm, respectively, indicating that the sericite crystal was stretched and deformed along the c-axis. Because the ionic bond is the interlayer force between the layers of sericite crystal, deformation is most prone along with the c-axis. Hence, the crystal deformation of sericite along the c-axis was also accompanied by dehydroxylation.

3.2.3. Microstructure Analysis

Raw sericite and roasted products at 850 °C, 950 °C, and 1050 °C were imaged under SEM to analyze the microstructure at different temperatures. Figure 7 illustrates that sericite was composed of several thin layers with obvious flaky structures. Fine flake debris adhered to the sample surface, and the diameter of most debris was less than 2 μm. It could be observed that the edge and fracture of particles were sharp. When the temperature increased from 850 °C to 1050 °C, the scaly particles on the surface melted, and the sharp fracture gradually became smooth. Figure 7c shows the small spherical particles formed at 950 °C. Sintering phenomena occurred at 1050 °C, and the flake particles were fused to the bump structure and closely attached to the surface. Meanwhile, metal ions were wrapped inside the molten silicate formed by sintering.

Table 2. The interplanar spacings of diffraction peaks of roasted products.

Crystal Planes	Interplanar Spacings/nm				
	Raw Sericite	700 °C	850 °C	900 °C	950 °C
(0 0 2)	0.9950	0.9973	1.0041	1.0041	1.0063
(0 0 4)	0.4982	0.4985	0.5029	0.5029	0.5035
(1 1 0)	0.4471	0.4505	0.4503	0.4498	0.4501
(−1 1 4)	0.3494	0.3500	0.3521	0.3517	0.3520
(0 0 6)	0.3323	0.3324	0.3355	0.3355	0.3357
(1 1 4)	0.3202	0.3205	0.3228	0.3227	0.3229
(0 2 5)	0.2992	0.2995	0.3028	0.3027	0.3031
(1 1 5)	0.2862	0.2865	0.2885	0.2886	0.2889
(−1 1 6)	0.2791	0.2794	0.2814	0.2814	0.2816
(0 0 8)	0.2493	0.2493	0.2516	0.2517	0.2518
(2 2 4)	0.1994	0.1994	0.2013	0.2013	0.2014
(1 3 9)	0.1647	0.1648	0.1666	0.1666	0.1666

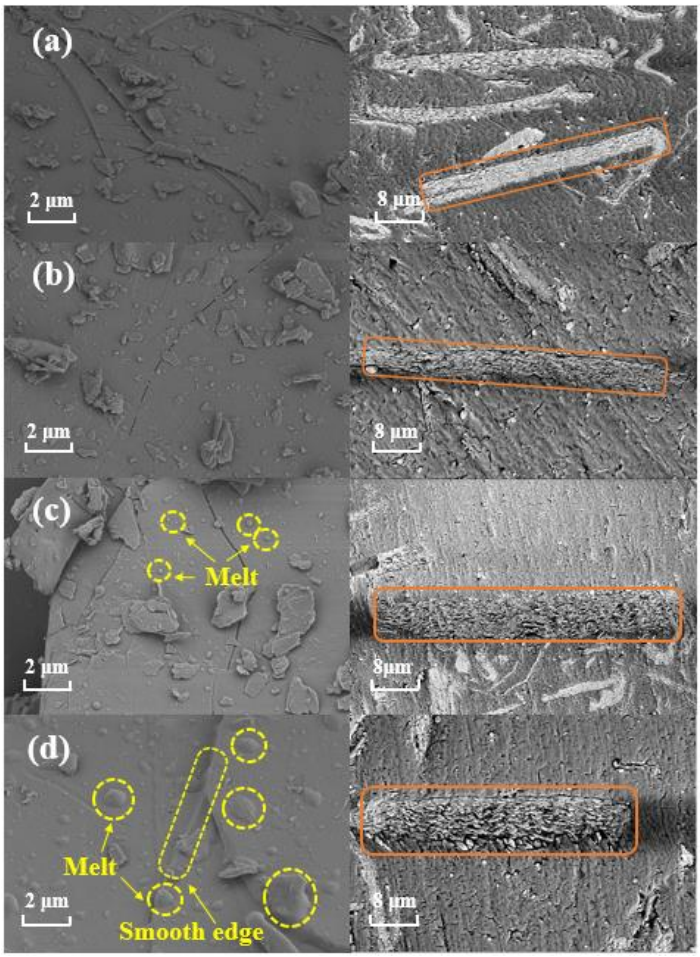

Figure 7. SEM images of sericite samples at different temperatures (raw ore (**a**), 850 °C (**b**), 950 °C (**c**), and 1050 °C (**d**)).

Taking the raw ore and roasted product at the highest temperature, Figure 8 shows the element distribution at 1050 °C. Si, O, Al, K, and Fe were the main constituent elements of sericite (the chemical formula is $K_{0.5–1}(Al,Fe,Mg)_2(SiAl)_4O_{10}(OH)_2 \cdot nH_2O$) [39,40]. Figure 8a illustrates those elements had a good correlation with particles. Figure 8b shows that Si, O, Al, K, and Fe also had good correlations. This showed there was no element loss before and after dehydroxylation. The inclusion of V elements in the melt leads to a poor

leaching effect of the sample [6,41]. Hence, too high a temperature should be avoided in the fluidized roasting process of shale.

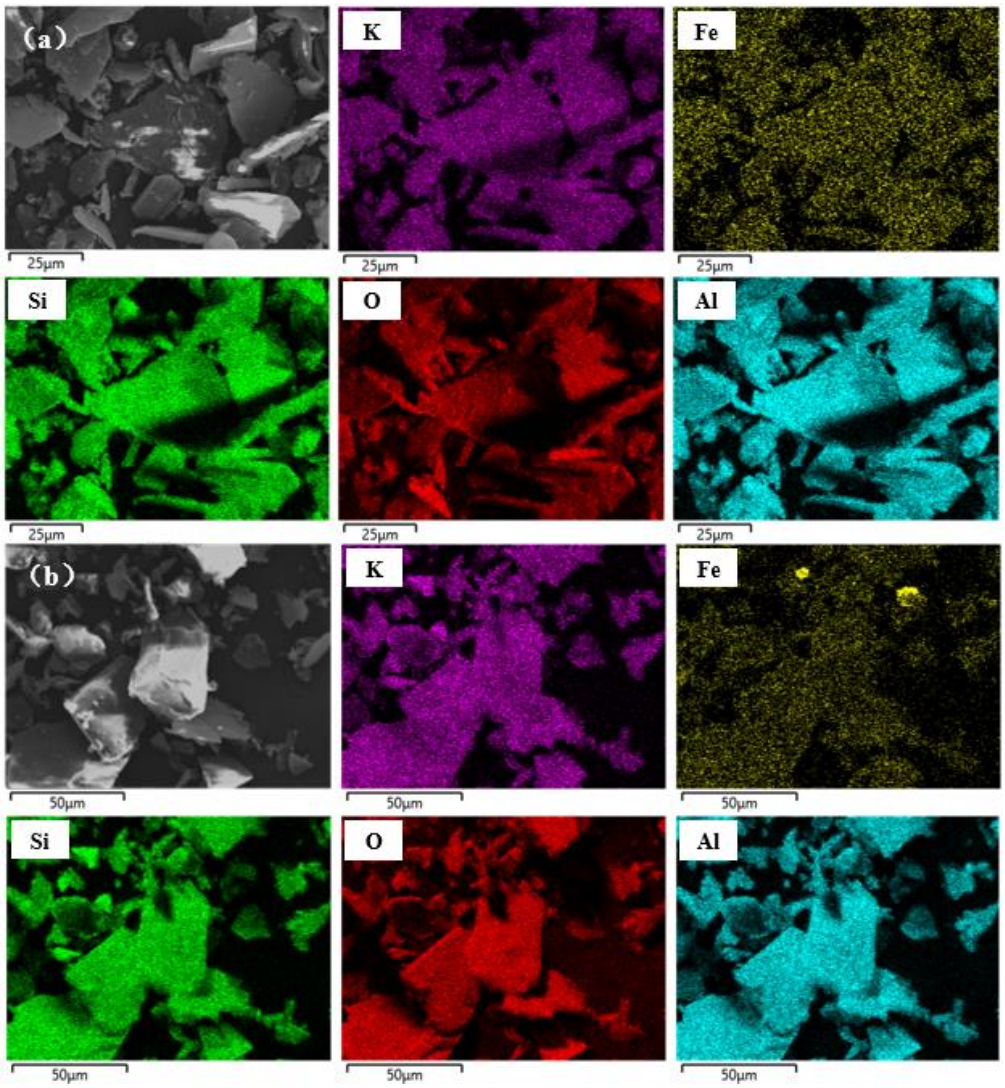

Figure 8. Element distribution on the sample surface at different temperatures (raw sericite (**a**), 1050 °C (**b**)).

3.3. DFT Calculation of Sericite Crystal

The DFT calculation could provide microcosmic and quantitative evidence for the analysis at an atomic scale [42]. Materials Studio software was used to estimate the microstructural transformation of V-bearing sericite during fluidized roasting [43].

3.3.1. Crystal Transformation during Dehydroxylation

Based on previous research, the best substitution position of the V^{3+} in the O-layer was determined [27]. Then, the crystal of V-bearing sericite was obtained as shown in Figure 9. An octahedral sheet with Al, V, Fe, and O is pinned between two tetrahedron sheets with Si and O, which formed a T-O-T layer structure. The T-layer is connected by the silica six-membered ring, and the O-layer is connected by the alumina six-membered ring [44]. Meanwhile, V^{3+} and Fe^{3+} usually replaced Al^{3+} by isomorphism in the O-layer [45,46]. Figure 10 shows the changes in sericite crystal before and after dehydroxylation. The calculated crystal parameters of raw ore were a = 0.8980 nm, b = 0.5177 nm, c = 2.1086 nm, α = 84.84°, β = 90.10°, and γ = 90.10°. In addition, the parameters of dehydroxylated sericite were a = 0.9116 nm, b = 0.5201 nm, c = 2.1181 nm, α = 85.78°, β = 90.49°, and γ = 89.86°.

The values of *a* and *c* elongated were found to be 0.0136 nm and 0.0095 nm, respectively. The expansion along the c-axis was due to the weak force between the crystal layers [47]. Moreover, the expansion along the a-axis and the change in *a*, *b*, and *c* were mainly due to the crystal transformation inside the crystal cell.

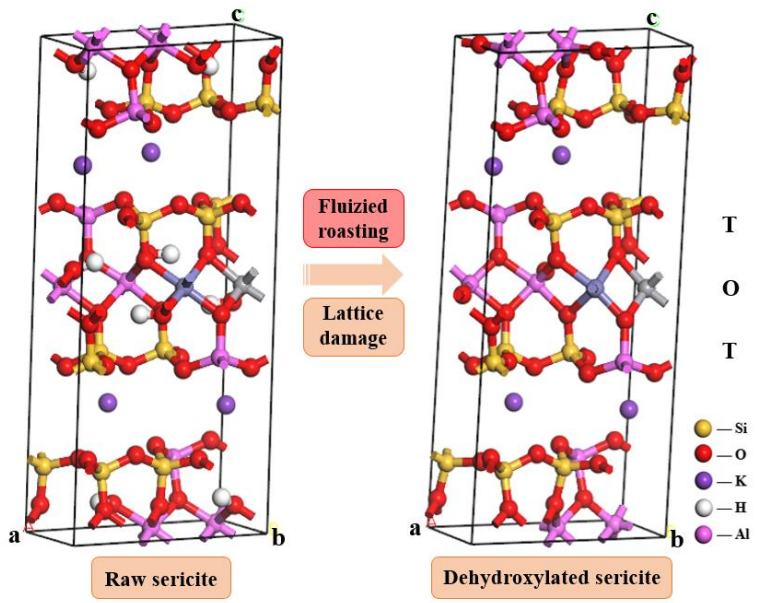

Figure 9. The crystal structure of sericite before and after dehydroxylation.

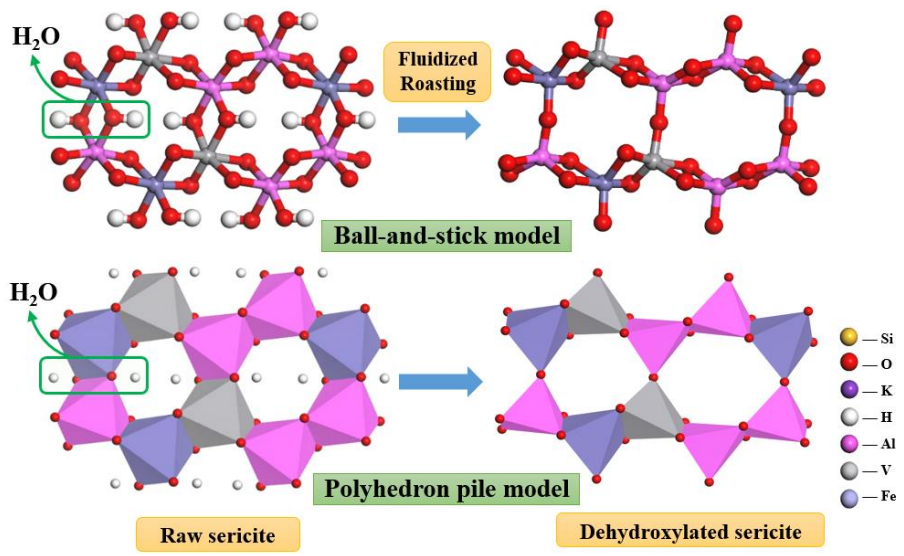

Figure 10. Structural change in sericite O-layer during dehydroxylation.

The sericite O-layer could be regarded as the repeated arrangement of two types of six-membered rings. In the sericite (0 0 1) surface, the crystal change in the O-layer before and after dehydroxylation is shown in Figure 11. This reaction occurred between adjacent metal ions (V^{3+} and Al^{3+}, and Fe^{3+} and Al^{3+}) [38]. An H_2O molecule was generated by the reaction of two −OH. Firstly, two connected O atoms were reduced to one between V^{3+} and Al^{3+}, and Fe^{3+} and Al^{3+}. Second, the coordination number of central ions decreased from 6 to 5, and the polyhedron pile model changed from hexa-coordinate to pentacoordinate. Finally, this reaction led to the rearrangement of electrons, the transformation of atomic sites, and the change in crystal parameters (a, b, c, α, β, and γ). These changes in microstructure correspond to the transformation of macro properties.

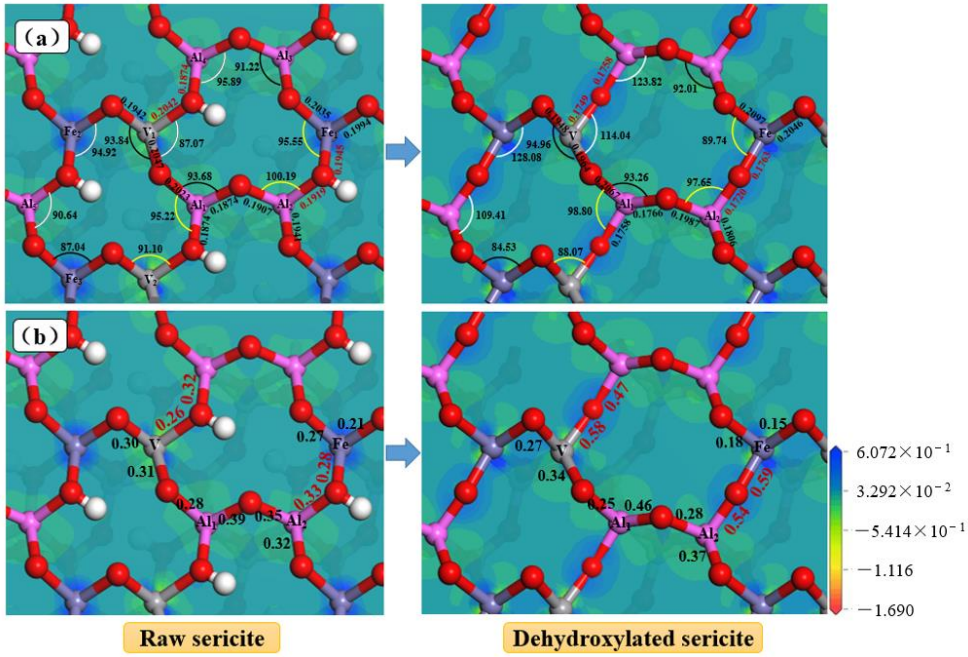

Figure 11. Parameters of chemical bonds in the sericite (0 0 1) surface (bond angle and bond length (**a**), Mulliken's overlap population (**b**)).

3.3.2. Analysis of Bond Parameters and Electron Population

Observed from the sericite (0 0 1) surface, the O-layer was composed of two kinds of six-membered rings with infinite repetition. Figure 11a illustrates the changes in bond length and bond angle, and Table 3 lists the distance between adjacent atoms. When -OH was removed between adjacent center atoms, two intermediate oxygen atoms became one. Near this position, the bond lengths of V-O, Al-O, and Fe-O (red mark) were shortened. However, other chemical bonds were increased from 0.1907~0.2037 nm to 0.1987~0.2097 nm, indicating that the strength of these chemical bonds decreased. Weakened chemical bonds make them easier to break when they react with acids. This is also one of the reasons why roasted samples are easier to leach [40,48].

Table 3. Distance between adjacent center atoms before and after dehydroxylation.

Distance/nm	V_1-Al_1	Al_1-Al_2	Al_2-Fe_1	Fe_1-Al_3	Al_3-Al_4	Al_4-V_1
Before	3.11	3.00	2.98	3.06	3.00	3.13
After	3.04	2.96	3.44	2.98	2.96	3.48
Distance/nm	V_1-Al_1	V_1-Fe_2	Fe_2-Al_5	Al_5-Fe_3	Fe_3-V_2	V_2-Al_1
Before	3.11	2.68	2.98	3.06	2.68	3.13
After	3.04	2.36	3.44	2.98	2.36	3.48

The distance between central atoms increased obviously, which increased to 0.35 nm and 0.46 nm for Al-V and Al-Fe, respectively. In contrast, the distance for V-Fe decreased to 0.32 nm. Moreover, in the ring, the bond angles near -OH pointing inside (with white mark in Figure 11a) expanded from 87.07~95.89° to 109.41~128.08°. However, the bond angles near −OH pointing outside (yellow mark) reduced from 91.10~100.19° to 88.07~98.80°. The other angles changed only by a little. The results above suggest that the original hexagonal structure has been seriously distorted and that two kinds of twisted six-membered rings were formed.

Mulliken's overlap population provides intuitive chemical information transformed from the wave function obtained by Molecular Orbital Theory. By distributing electronic charges to atoms, atomic orbitals, and chemical bonds, it is used to study the transfer of

electrons in molecules, the polarity of molecules, as well as the type and strength of chemical bonds, etc. [49,50]. Additionally, it is dimensionless and has no physical meaning [51]. According to Mulliken's overlap populations of bonds and atoms, as well as atomic net charges (Figure 11b), electronic structures and bonding characters were discussed to clarify the transformation between sericite and dehydroxylated products. Mulliken's overlap populations in the raw ore were all about 0.3, indicating that each bond presented the nature of the ionic bond and has similar strengths. The most obvious change occurred at the dehydroxylation site. When two O atoms were connected between the V and Al atoms—V-O and Al-O—Mulliken's overlap populations were 0.26 and 0.32. After roasting, there was only one O atom between two atoms, and the populations of V-O and Al-O increased to 0.58 and 0.47, respectively. The law between Al and Fe was the same. This indicated that newly generated bonds tend to be covalent bonds with stronger strength. It should be noted that Mulliken's overlap populations of some V-O, Al-O, and Fe-O decreased from 0.30, 0.35, and 0.27 to 0.27, 0.25, and 0.18, respectively. This indicated that their covalency was weakened and that they were easier to destroy. Furthermore, Mulliken's overlap populations of atoms before and after dehydroxylation are presented in Table 4. V^{3+}, Fe^{3+}, and Al^{3+} in the O-layer were electron deficiency sites and the O atoms were multi-electron sites. After fluidized roasting, the electrons of the V^{3+} increased from 11.72 to 11.81, and Fe^{3+} increased from 7.04 to 7.13, while the electrons of the Al^{3+} decreased from 1.31~1.33 to 1.25. These results indicated electron transfer from Al^{3+} to O atoms rather than to V^{3+} and Fe^{3+} ions.

Table 4. Mulliken population of atoms before and after dehydroxylation.

Ions	State	s Orbital	p Orbital	d Orbital	Total	Charge/e
V_1	Before	2.25	6.17	3.31	11.72	1.28
	After	2.20	6.21	3.40	11.81	1.19
Al_1	Before	0.50	0.81	-	1.31	1.69
	After	0.47	0.78	-	1.25	1.75
Al_2	Before	0.51	0.81	-	1.33	1.67
	After	0.46	0.79	-	1.25	1.75
Fe_1	Before	0.25	0.24	6.54	7.04	0.96
	After	0.26	0.35	6.52	7.13	0.87

In summary, raw ore has a stable structure in which each parameter—bond angle, length, and population—is pretty close, and the O-layer is composed of an approximate hexagonal structure. However, after fluidized roasting, the metal ions in the sericite O-layer changed from hexa-coordinate to pentacoordinate. With the rearrangement of electrons, some bond lengths increased or decreased, and the bond strength also increased or decreased. This indicated that roasting would lead to forming more unstable chemical bonds and reducing crystal stability inside sericite crystals. This should be the reason vanadium and other metal ions are easier to leach out in the roasted product.

4. Conclusions

The transformation of sericite to dehydroxylated sericite was the main reaction during fluidized roasting. TG-MS revealed that this reaction could occur at 650~960 °C. When sericite was roasted at 900 °C for 2 h, their hydroxyls were completely removed. The calculations showed that -OHs were removed between V^{3+} and Al^{3+}, and between Fe^{3+} and Al^{3+} in the sericite O-layer, which turned the hexa-coordinate structure of V^{3+}, Al^{3+}, and Fe^{3+} into pentacoordinate. It showed that their stable octahedron structure was destroyed into an unstable hexahedron structure. Meanwhile, the electrons were rearranged. Mulliken's overlap populations were increased from 0.26~0.36 to 0.47~0.59. On the sericite (0 0 1) surface, the angles changed from 87.04~100.19° to 84.53~128.08°. In addition, Mulliken's overlap populations of some other V-O, Al-O, and Fe-O decreased from 0.30 to 0.27, from 0.35 to 0.25, and from 0.27 to 0.18, respectively, indicating that their ionicities

were weakened. Some bond lengths were increased; therefore, the strength of the chemical bonds was reduced and the bonds were fragile. The distorted hexahedron structure with fragile chemical bonds in the O-layer explained the destructive effect of fluidized roasting on the stability of V-bearing sericite.

Author Contributions: Conceptualization, Y.H. and J.J.; methodology, J.J.; software and validation, Z.B.; data curation and writing—original draft preparation, Z.B.; writing—review and editing, Y.S. and Q.Z.; visualization, Q.Z.; funding acquisition, J.J. All authors have read and agreed to the published version of the manuscript.

Funding: This research is funded by National Key Research and Development Program of China (grant No. 2020YFC1909704) and the Fundamental Research Funds for the Central Universities (No. N2201001).

Data Availability Statement: Not applicable.

Conflicts of Interest: The authors declare no conflict of interest.

References

1. Luo, Y.; Che, X.; Cui, X.; Zheng, Q.; Wang, L. Selective leaching of vanadium from V-Ti magnetite concentrates by pellet calcification roasting-H_2SO_4 leaching process. *Int. J. Min. Sci. Technol.* **2021**, *31*, 507–513. [CrossRef]
2. Li, H.-Y.; Wang, C.; Lin, M.; Guo, Y.; Xie, B. Green one-step roasting method for efficient extraction of vanadium and chromium from vanadium-chromium slag. *Powder Technol.* **2019**, *360*, 503–508. [CrossRef]
3. Cai, Z.; Feng, Y.; Li, H.; Zhou, Y. Selective Separation and Extraction of Vanadium(IV) and Manganese(II) from Co-leaching Solution of Roasted Stone Coal and Pyrolusite via Solvent Extraction. *Ind. Eng. Chem. Res.* **2013**, *52*, 13768–13776. [CrossRef]
4. Chen, T.; Li, Q.; Li, Q.; Wu, Z.; Dong, G.; Wan, J. Application of PVC as Novel Roasting Additive in Vanadium Extraction from Stone Coal. *Mining, Met. Explor.* **2019**, *36*, 931–939. [CrossRef]
5. Chen, B.; Bao, S.; Zhang, Y. Synergetic strengthening mechanism of ultrasound combined with calcium fluoride towards vanadium extraction from low-grade vanadium-bearing shale. *Int. J. Min. Sci. Technol.* **2021**, *31*, 1095–1106. [CrossRef]
6. Yuan, Y.; Zhang, Y.; Hu, P. Formation mechanism and control method of the silicate minerals-based coating (SMC) in blank roasting process of vanadium-bearing shale. *Colloids Surfaces A: Physicochem. Eng. Asp.* **2020**, *592*, 124535. [CrossRef]
7. Dong, Y.-B.; Liu, Y.; Lin, H.; Liu, C.-J. Improving vanadium extraction from stone coal via combination of blank roasting and bioleaching by ARTP-mutated Bacillus mucilaginosus. *Trans. Nonferrous Met. Soc. China* **2019**, *29*, 849–858. [CrossRef]
8. Kang, Q.; Zhang, Y.; Bao, S. Cleaning method of vanadium precipitation from stripped vanadium solution using oxalic acid. *Powder Technol.* **2019**, *355*, 667–674. [CrossRef]
9. Zhu, Y.-G.; Zhang, G.-F.; Feng, Q.-M.; Lu, Y.-P.; Ou, L.-M.; Huang, S.-J. Acid leaching of vanadium from roasted residue of stone coal. *Trans. Nonferrous Met. Soc. China* **2010**, *20*, s107–s111. [CrossRef]
10. Zhao, Y.; Wang, W.; Zhang, Y.; Song, S.; Bao, S. In-situ investigation on mineral phase transition during roasting of vanadium-bearing stone coal. *Adv. Powder Technol.* **2017**, *28*, 1103–1107. [CrossRef]
11. Zhao, Y.; Zhang, Y.; Liu, T.; Chen, T.; Bian, Y.; Bao, S. Pre-concentration of vanadium from stone coal by gravity separation. *Int. J. Miner. Process.* **2013**, *121*, 1–5. [CrossRef]
12. Long, S.; Feng, Q.; Zhang, G.; He, N. Recovery of vanadium from alkaline leaching solution from roasted stone coal. *ScienceAsia* **2014**, *40*, 69–72. [CrossRef]
13. Zhao, Y.; Zhang, Y.; Song, S.; Chen, T.; Bao, S. Behaviors of impurity elements Ca and Fe in vanadium-bearing stone coal during roasting and its control measure. *Int. J. Miner. Process.* **2016**, *148*, 100–104. [CrossRef]
14. Shi, Q.; Zhang, Y.; Liu, T.; Huang, J. Vanadium Extraction from Shale via Sulfuric Acid Baking and Leaching. *JOM* **2018**, *70*, 1972–1976. [CrossRef]
15. Chen, F.; Zhang, Y.; Huang, J.; Liu, T.; Xue, N. Mechanism of Enhancing Extraction of Vanadium from Stone Coal by Roasting with MgO. *Minerals* **2017**, *7*, 33. [CrossRef]
16. Cheng, X.; Chen, K.; Cheng, H.; Zhang, L. Extraction of vanadium from Chinese black shale by roasting using Na_2CO_3-$BaSO_4$ mixture addition. In Proceedings of the International Conference on Renewable Energy and Environmental Technology, Phuket, Thailand, 21–22 September 2013; pp. 3912–3915.
17. Zhang, Y.-M.; Bao, S.-X.; Liu, T.; Chen, T.-J.; Huang, J. The technology of extracting vanadium from stone coal in China: History, current status and future prospects. *Hydrometallurgy* **2011**, *109*, 116–124. [CrossRef]
18. Wang, M.-Y.; Wang, X.-W.; Shen, J.-F.; Wu, R.-N. Extraction of vanadium from stone coal by modified salt-roasting process. *J. Central South Univ. Technol.* **2011**, *18*, 1940–1944. [CrossRef]
19. Wang, F.; Zhang, Y.-M.; Liu, T.; Huang, J.; Zhao, J.; Zhang, G.; Liu, J. Comparison of direct acid leaching process and blank roasting acid leaching process in extracting vanadium from stone coal. *Int. J. Miner. Process.* **2014**, *128*, 40–47. [CrossRef]
20. Wang, D.; Jiang, Y.; Zhu, Z.; Yin, W.; Asawa, K.; Choi, C.-H.; Drelich, J.W. Contact Line and Adhesion Force of Droplets on Concentric Ring-Textured Hydrophobic Surfaces. *Langmuir* **2020**, *36*, 2622–2628. [CrossRef] [PubMed]

21. Yang, X.; Feng, Y.; Li, H.; Du, Z. Optimization Mechanism of Additive of Composite Sodium Salts on Vanadium Oxidation of Siliceous Shale. *Minerals* **2017**, *7*, 103. [CrossRef]
22. Wang, B.; Liu, T.; Zhang, Y.; Huang, J. Effect of CaF_2/CaO Composite Additive on Roasting of Vanadium-Bearing Stone Coal and Acid Leaching Kinetics. *Minerals* **2017**, *7*, 43. [CrossRef]
23. Cai, Z.; Feng, Y.; Li, H.; Du, Z.; Liu, X. Co-recovery of manganese from low-grade pyrolusite and vanadium from stone coal using fluidized roasting coupling technology. *Hydrometallurgy* **2012**, *131–132*, 40–45. [CrossRef]
24. Zhang, X.; Han, Y.; Sun, Y.; Lv, Y.; Li, Y.; Tang, Z. An Novel Method for Iron Recovery from Iron Ore Tailings with Pre-Concentration Followed by Magnetization Roasting and Magnetic Separation. *Miner. Process. Extr. Met. Rev.* **2019**, *41*, 117–129. [CrossRef]
25. Tang, Z.; Zhang, Q.; Sun, Y.; Gao, P.; Han, Y. Pilot-scale extraction of iron from flotation tailings via suspension magnetization roasting in a mixture of CO and H2 followed by magnetic separation. *Resour. Conserv. Recycl.* **2021**, *172*, 105680. [CrossRef]
26. Bai, Z.; Han, Y.; Jin, J.; Sun, Y.; Zhou, Z. Extraction of vanadium from black shale by novel two-step fluidized roasting process. *Powder Technol.* **2022**, *408*, 117745. [CrossRef]
27. Zheng, Q.; Zhang, Y.; Liu, T.; Huang, J.; Xue, N.; Shi, Q. Optimal Location of Vanadium in Muscovite and Its Geometrical and Electronic Properties by DFT Calculation. *Minerals* **2017**, *7*, 32. [CrossRef]
28. Sun, Y.; Zhu, X.; Han, Y.; Li, Y.; Gao, P. Iron recovery from refractory limonite ore using suspension magnetization roasting: A pilot-scale study. *J. Clean. Prod.* **2020**, *261*, 121221. [CrossRef]
29. Liu, X.; Gao, P.; Yuan, S.; Lv, Y.; Han, Y. Clean utilization of high-iron red mud by suspension magnetization roasting. *Miner. Eng.* **2020**, *157*, 106553. [CrossRef]
30. Zhang, X.; Han, Y.; Sun, Y.; Li, Y. Innovative utilization of refractory iron ore via suspension magnetization roasting: A pilot-scale study. *Powder Technol.* **2019**, *352*, 16–24. [CrossRef]
31. Zheng, Q.; Zhang, Y.; Liu, T.; Huang, J.; Xue, N. Removal Process of Structural Oxygen from Tetrahedrons in Muscovite during Acid Leaching of Vanadium-Bearing Shale. *Minerals* **2018**, *8*, 208. [CrossRef]
32. Zheng, Q.; Zhang, Y.; Xue, N. Migration and coordination of vanadium separating from black shale involved by fluoride. *Sep. Purif. Technol.* **2021**, *266*, 118552. [CrossRef]
33. Yang, X.L.; Feng, Y.L.; Li, H.R.; Du, Z.W.; Liu, P.W. Effect of preroasting on the preoxidation of vanadium in high-carbon stone coal. *Asia-Pacific, J. Chem. Eng.* **2018**, *13*, e2216. [CrossRef]
34. Liu, L.; Gong, Z.; Wang, Z.; Zhang, H. Study on combustion and emission characteristics of chars from low-temperature and fast pyrolysis of coals with TG-MS. *Environ. Eng. Res.* **2019**, *25*, 522–528. [CrossRef]
35. Zhang, H.; Dou, B.; Zhang, H.; Li, J.; Ruan, C.; Wu, C. Study on non-isothermal kinetics and the influence of calcium oxide on hydrogen production during bituminous coal pyrolysis. *J. Anal. Appl. Pyrolysis* **2020**, *150*, 104888. [CrossRef]
36. Luo, L.; Liu, J.; Zhang, H.; Ma, J.; Wang, X.; Jiang, X. TG-MS-FTIR study on pyrolysis behavior of superfine pulverized coal. *J. Anal. Appl. Pyrolysis* **2017**, *128*, 64–74. [CrossRef]
37. Yuan, Y.-Z.; Zhang, Y.-M.; Liu, T.; Chen, T.-J. Comparison of the mechanisms of microwave roasting and conventional roasting and of their effects on vanadium extraction from stone coal. *Int. J. Miner. Met. Mater.* **2015**, *22*, 476–482. [CrossRef]
38. Yuan, Y.; Zhang, Y.; Liu, T.; Hu, P.; Zheng, Q. Optimization of microwave roasting-acid leaching process for vanadium extraction from shale via response surface methodology. *J. Clean. Prod.* **2019**, *234*, 494–502. [CrossRef]
39. Bárcena, J.L.; Urbina, M.; Rowlands, A.P.; Beneitez, P.; Millán, A.; Calderón, T. Basic Thermoluminescence Properties of Micas: Muscovite, Sericite and Phlogopite. *Radiat. Prot. Dosim.* **1999**, *84*, 289–292. [CrossRef]
40. Xu, X.; Ding, H.; Liang, N.; Wang, Y.; Yan, W. Effects of Heat Treatment on Crystal Structure and Reactivity of Sericite. In Proceedings of the 6th East Asian Symposium on Functional Ion Application Technology/International Forum on Ecological Environment Functional Materials and Industry, Shanghai, China, 24–25 September 2010; p. 113.
41. Hu, Y.-J.; Zhang, Y.-M.; Bao, S.-X.; Liu, T. Effects of the mineral phase and valence of vanadium on vanadium extraction from stone coal. *Int. J. Miner. Met. Mater.* **2012**, *19*, 893–898. [CrossRef]
42. Xie, R.; Zhu, Y.; Liu, J.; Li, Y. The flotation behavior and adsorption mechanism of a new cationic collector on the separation of spodumene from feldspar and quartz. *Sep. Purif. Technol.* **2021**, *264*, 118445. [CrossRef]
43. Xie, R.; Zhu, Y.; Liu, J.; Li, Y. Flotation behavior and mechanism of α-bromododecanoic acid as collector on the flotation separation of spodumene from feldspar and quartz. *J. Mol. Liq.* **2021**, *336*, 116303. [CrossRef]
44. Yu, C.J.; Choe, S.H.; Jang, Y.M.; Jang, G.H.; Pae, Y.H. First-principles study of organically modified muscovite mica with ammonium (NH) or methylammonium (CHNH) ion. *J. Mater. Sci.* **2016**, *51*, 10806–10818. [CrossRef]
45. Ferraris, G.; Ivaldi, G. Structural features of micas. In *Micas: Crystal Chemistry and Metamorphic Petrology*; Mineralogical Society of America: Chantilly, VA, USA, 2002; pp. 117–153.
46. Brigatti, M.F.; Kile, D.E.; Poppi, M. Crystal Structure and Crystal Chemistry of Lithium-Bearing Muscovite-2M1. *Can. Miner.* **2001**, *39*, 1171–1180. [CrossRef]
47. Zanazzi, P.F.; Pavese, A. Behavior of micas at high pressure and high temperature. In *Micas: Crystal Chemistry and Metamorphic Petrology*; Mineralogical Society of America: Chantilly, VA, USA, 2002; pp. 99–116.
48. Zheng, Q.; Zhang, Y.; Xue, N. Enhancing Effect of Vanadium Releasing Efficiently from Lattice in Black Shale by Thermal Activation. *Colloids Surf. A Physicochem. Eng. Asp.* **2022**, *651*, 129773. [CrossRef]

49. Jin, J.; Miller, J.D.; Dang, L.X. Molecular dynamics simulation and analysis of interfacial water at selected sulfide mineral surfaces under anaerobic conditions. *Int. J. Miner. Process.* **2014**, *128*, 55–67. [CrossRef]
50. Terra, J.; Jiang, M.; Ellis, D.E. Characterization of electronic structure and bonding in hydroxyapatite: Zn substitution for Ca. *Philos. Mag. A-Phys. Condens. Matter Struct. Defect Mech. Prop.* **2002**, *82*, 2357–2377. [CrossRef]
51. Louis-Achille, V.; De Windt, L.; Defranceschi, M. Electronic structure of minerals: The apatite group as a relevant example. *Int. J. Quantum Chem.* **2000**, *77*, 991–1006. [CrossRef]